Research Square

Preprints are preliminary reports that have not undergone peer review.
They should not be considered conclusive, used to inform clinical practice,
or referenced by the media as validated information.

Network analysis of two-phase blood flow in kidney glomeruli

Anton Glazkov

anton.glazkov@kaust.edu.sa

King Abdullah University of Science and Technology (KAUST)

Peter Schmid

King Abdullah University of Science and Technology (KAUST)

Diego Rossinelli

Stanford University

Dominik Obrist

University of Bern

Research Article

Keywords: glomerulus, hemodynamics, microcirculation, network analysis, filtration, kidney

Posted Date: November 23rd, 2026

DOI: https://doi.org/10.21203/rs.3.rs-11336303/v1

License: This work is licensed under a Creative Commons Attribution 4.0 International License.
Read Full License

Additional Declarations: No competing interests reported.

Network analysis of two-phase blood flow in kidney glomeruli

Anton Glazkov[1*], Peter Schmid[1], Diego Rossinelli[3], Dominik Obrist[2]

[1*]Department of Mechanical Engineering, Division of Physical Sciences and Engineering (PSE), King Abdullah University of Science and Technology (KAUST), Thuwal, 23955, Saudi Arabia.

[2]ARTORG Center for Biomedical Engineering Research, University of Bern, Freiburgstrasse 3, Bern, 3010, Switzerland.

[3]Institute for Computational and Mathematical Engineering (ICME), Center for Turbulence Research, Stanford University, Stanford, 94305-3024, CA, United States.

*Corresponding author(s). E-mail(s): anton.glazkov@kaust.edu.sa;
Contributing authors: peter.schmid@kaust.edu.sa; rossinel@stanford.edu;
dominik.obrist@unibe.ch;

Abstract

Glomeruli are the functional units responsible for the filtration of the blood in the kidney. Using network theory, prior analysis of the interconnected blood vessels making up the glomerulus has indicated the existence of a topologically shortest path that was invariant to the size of the network. At the same time, it is known that red blood cells (RBCs) in micro-circulation environments propagate in ways that lead to heterogeneous distributions of RBCs within microvasculature. Using eleven newly available skeletonised glomeruli from the NCCR Kidney dataset, this study aims to combine these two observations by linking the topology to the flow of the blood plasma, the propagation of RBCs, and the effects of these on the filtration efficiency of the glomerulus. An initial characterisation of the networks confirms the invariance of the minimum-edge shortest path to network size. This is then extended to three further definitions of shortest path, one by length and two *greedy* paths based on the local flow at bifurcating capillaries, that are also observed to be insensitive to the size of the network. We add RBCs to the flow and their propagation is compared to passive particles (PPs) that distribute homogeneously in the network. A clear heterogeneous distribution of RBCs is observed in the vicinity of the the previously computed shortest paths, while the transit times form a probability density function that imprints features of the topology onto the propagation dynamics for both RBCs and PPs. We conclude by conducting an analysis of the filtration rate and filtration efficiency. In all cases, the former is higher for RBCs than for PPs in all networks, while, in the latter, eight out of eleven networks see a gain in filtration efficiency. A Monte-Carlo sensitivity analysis shows that these results are robust to perturbations to the vessel diameters.

Keywords: glomerulus, hemodynamics, microcirculation, network analysis, filtration, kidney

1 Introduction

Glomeruli are microscopic tufts of capillaries, forming a part of the functional units of a kidney.

They are approximately $200 - 225\,\mu m$ in diameter in humans and $70\,\mu m$ in mice (Nyengaard and Bendtsen (1992); Terasaki et al. (2020)), and are embedded within *Bowman's capsule*, which collects the primary urine/filtrate. Unlike most of the capillaries in the body, the primary function of these is not oxygen and nutrient supply to tissues, but controlled filtration of solutes and fluid from the blood plasma. This filtration barrier consists of an endothelium that is fenestrated across 20% of its surface by holes between $50 - 100\,nm$ in diameter, to retain the cellular components of the blood, followed by a glomerular basement membrane and a layer of podocyte cells which effectively form a barrier to plasma proteins. Approximately 20% of cardiac output is is supplied to the kidneys, with an effective $600\,mL/min$ renal plasma flow, and a $120\,mL/min$ glomerular filtration rate in humans (see Feher (2017) for full details). Red blood cells (RBCs) hinder filtration by obscuring the surface area of the glomerular capillaries exposed to the blood plasma.

Earlier work by Wahl et al. (1984, 2004) introduced and applied network theory to describe the capillary tufts of glomeruli quantitatively through graph statistics, and to evaluate their physiology. These studies indicated that the graphs were non-planar networks and that the shortest paths between the afferent (inlet) and efferent (outlet) nodes were independent of the number of vessels and branch points in the glomerulus, with a hypothesis advanced that the glomerular network develops by branching out from this shortest path. While this earlier analysis had to resort to analysing the glomeruli by histology sections, recent developments in imaging with transmission electron microscopy enabled Terasaki et al. (2020) to extract and reconstruct 12 glomerular networks at high resolution. From the skeletonized networks they were able to confirm non-planarity, determined that the shortest paths underwent between 6 and 12 bifurcations between the inlet and outlet of the network and were independent of glomerular network size, and that the shortest path was primarily concentrated within the hemisphere of glomerulus containing the afferent and efferent vessels.

At the same time, it is well-known that blood flow in microcirculation is highly heterogeneous (Hudetz (1997)). Obrist et al. (2010) showed that the heterogeneous distribution of RBCs in capillary networks is caused by the Zweifach–Fung (ZF) effect which describes the non-proportional RBC partitioning at diverging bifurcations (Fung and Zweifach (1971); Pries and Secomb (2005)). While hematocrit heterogeneity improves the stability of blood perfusion in normal microvasculature, for example in the brain (Schmid et al., 2019), Goligorsky (2023) hypothesized that the mechanisms underpinning RBC partitioning, and the clear presence of this *shortest path*, should also lead to heterogeneous hematocrit distributions in glomerular capillary networks, with implications for filtration efficiency, because high local hematocrit levels have an obstructive effect, whereas cell-depleted regions of the glomerulus allow for better filtration.

In this work, we hypothesize that this hematocrit heterogeneity, in association with the specific structure of the glomerular networks, leads to enhanced overall filtration efficiency of glomeruli. To test this hypothesis, we will evaluate 11 new mouse glomeruli (different from the glomeruli studied by Terasaki et al. (2020)). Building upon the earlier work of Terasaki et al. (2020), we will define two new kinds of shortest path that take into account the mean plasma flow. We will then evaluate these networks under evolving flow conditions, in the context of a two-phase flow model, with and without the ZF-effect. We will show that the ZF-effect indeed leads to (a) elevated hematocrit levels in the shortest vascular pathways, (b) cell-depleted capillaries in the rest of the glomerulus, and (c) improved urine filtration rates according to performance and efficiency estimates based upon Starling's law for filtration (Woodcock and Woodcock, 2012; Starling, 1896).

Additional materials providing details of the numerical model, the validation, and other points of interest are in the attached supplementary material.

2 Methods

2.1 Computational modelling

The computational modelling of the two-phase plasma-RBC system in this work follows the approach detailed in Schmid et al. (2019); Obrist et al. (2010). Each component of the computational model is briefly outlined below, while

more details of the model are reserved for the supplementary material.

2.1.1 Plasma flow model

At the low Reynolds numbers observed in microcirculation, the Navier-Stokes equations for the blood plasma simplify to the Stokes equations. Although some older studies (e.g. Drumond and Deen (1991)) report pulsatile flow in the glomerulus, we assume here quasi-steady plasma flow because the associated Womersley number is well below unity. For the network of fine capillaries of the glomerulus the flow is largely one-dimensional and the governing equations can be recast as a linear system of equations using Kirchoff's laws for equivalent electric circuits.

To this end, we assume that the flow of plasma in a capillary is driven by a pressure difference at the endpoints of the vessel, with the flow resistance determined by viscous forces from the parabolic Poiseuille profile within the plasma-filled portions of the vessel, and annular Couette-like profiles in the narrow gaps between capillary wall and RBCs. From the mathematical point of view, the flow rate q_{ij} between two nodes i and j, which are joined by k edges, can be written as

$$q_{ij} = \sum_k q_{ijk} = \sum_k T^e_{ijk}(p_i - p_j), \tag{1}$$

Here p_i and p_j are the pressures at the vessel endpoints i and j, and T^e_{ijk} denotes the *effective transmissibility* of a given vessel which is computed as

$$T^e_{ijk} = \frac{T_{ijk}}{\mu_{\mathrm{e,rel}}}, \quad T_{ijk} = \frac{\pi r^4_{ijk}}{8\mu l_{ijk}} \tag{2}$$

where r_{ijk} and l_{ijk} are vessel radius and length, and μ is the plasma viscosity. The *relative effective viscosity* $\mu_{\mathrm{e,rel}}$ accounts for the non-Newtonian behavior due to the Fåhraeus-Lindqvist effect. Here, we use the empirical model described in Pries et al. (1992) which estimates the relative effective viscosity in function of the vessel diameter $\delta = 2r_{ijk}$ and the discharge hematocrit H_D,

$$\mu_{\mathrm{e,rel}} = \mu_{\mathrm{e,rel}}(\delta, H_D) \tag{3}$$

Note that the discharge hematocrit H_D is not readily available for each individual vessel. Therefore, it is estimated *ad hoc* from the tube hematocrit H_T using the empirical law for the Fåhraeus effect described in Pries et al. (1992). Finally, the tube hematocrit H_T of a particular vessel is computed as

$$H_T = \frac{N^{\mathrm{RBC}}_{ijk} V_{\mathrm{RBC}}}{\pi r^2_{ijk} l_{ijk}} \tag{4}$$

where N^{RBC}_{ijk} is the number of RBCs in the vessel (see the following section on RBC dynamics) and V_{RBC} is the mean corpuscular volume of a murine RBC.

Mass conservation is enforced at every node j by

$$\sum_i q_{ij} = \begin{cases} q^{\mathrm{i/o}} & \text{at inlet/outlet} \\ 0 & \text{otherwise.} \end{cases} \tag{5}$$

In combination with appropriately chosen boundary conditions, which will be discussed below, eqs. (1) to (5) yield the sparse linear system of equations

$$\mathbf{Tp} = \mathbf{q}, \tag{6}$$

for the unknown vector of all nodal pressures $\mathbf{p} = \{p_j\}$, and with a non-zero right-hand side $\mathbf{q}$ comprising inlet or outlet flow rate. The matrix $\mathbf{T}$ is a sparse matrix containing the effective transmissibilities T^e_{ijk}. Therefore, the system eq. (6) must be solved, every time T^e_{ijk} is updated, e.g., due to a change in H_T.

2.1.2 Boundary conditions

The pressure at the outlet node is set to $p_{\mathrm{out}} = 0$. At the inlet, a volumetric inflow rate $q^i = Q_{\mathrm{in}}$ is imposed via the right-hand side of eq. (6). Alternatively, an inlet pressure p_{in} can be imposed, which, with $p_{\mathrm{out}} = 0$, effectively defines a perfusion pressure drop across the network. While the perfusion pressure may be a more physiologically relevant boundary condition, we prefer here to impose a constant inflow. This allows for consistent flow through times, which make the transit time estimates more comparable and match closely with the formulation of the underlying hypothesis of this work.

However, the choice of the inflow boundary condition has a direct effect on the filtration rate

of the network, because higher or lower pressure at the inlet will lead to correspondingly higher or lower filtration especially in the first few vessels. We will address this problem by normalizing our metric for the filtration rate with respect to the mean mechanical power $\overline{P_{\text{in}}} = \overline{p_{\text{in}} Q_{\text{in}}}$ applied to the network. Furthermore, we also use the inflow rate Q_{in} to normalize the time variable t by dividing it by the *network turnover time* defined as $\tau = V_{\text{net}}/Q_{\text{in}}$, where V_{net} is the total network volume.

2.1.3 RBC dynamics

RBCs are modelled as individual particles that are transported with the plasma flow. As with prior numerical simulations Obrist et al. (2010); Schmid et al. (2015), the propagation of an RBC across bifurcations is governed by a bifurcation law designed to reproduce the ZF-effect.

Whenever an RBC arrives at a bifurcation, the bifurcation law assigns this RBC to the branching vessel with the momentarily highest outflow velocity. In addition, the bifurcation law allows RBCs to enter a new vessel only if there is enough space available. We determine this by computing the height of a cylinder with radius r_{ijk} and volume V_{rbc} with the centre of mass at the location of the next RBC, and insisting that the separation length between the two RBC positions is at least the height of this cylinder. In this way, wider vessels allow for closer stacking than in narrower vessels. Averaging the RBC dynamics over many bifurcation events, this bifurcation law converges toward the classical sigmoid curves of Pries et al. (1990)), and it reproduces the self-regulation effect (Fung (1973); Pozrikidis (2009); Schmid et al. (2015); Obrist et al. (2010)) which, on average, balances the flow rates at diverging bifurcations.

The variable N_{ijk}^{RBC} keeps track of the number of RBCs within a vessel. This number is increased or decreased whenever and RBC enters or leaves that vessel.

The individual RBCs are advected with the velocity u_{rbc}. According to the Fåhraeus effect, this velocity is higher than the mean blood flow velocity. It can be estimated as

$$u_{\mathbf{rbc}} = u_{ijk} \frac{H_D}{H_T} = \frac{q_{ijk}}{\pi r_{ijk}^2} \frac{H_D}{H_T} \tag{7}$$

where q_{ijk} is given by eq. (1), the tube hematocrit H_T is calculated from eq. (4), and the discharge hematocrit H_D is estimated using the empirical law by Pries et al. (1992) as described before.

Initially, RBCs are injected at the inlet of the network, and so they must be propagated to remove the initial transients and for the RBCs to redistribute to a physical configuration. To maintain a constant network hematocrit, all RBCs that leave the network through the outlet are immediately returned into the network through the inlet.

As the redistribution of RBCs within the network takes time, the simulations are run for 15 s, or equivalently approximately 20τ network turnover times – only for the '*glom6*' case was this 13τ, before network metrics are evaluated following a further simulation over an additional 20 s ($\approx 27\tau$).

2.1.4 Passive particle (PP) dynamics

The RBC dynamics described above lead to the well-known heterogeneity in the RBC distribution across capillary networks. In order to understand the effect of this heterogeneity on the various network metrics of interest, such as RBC transit times and network filtration rate, we must construct a proxy model that maintains the Fåhraeus and the Fåhraeus-Lindqvist effects, but that eliminates the heterogeneous RBC distribution. To address this we introduce passive particles (PPs). These act in every way as RBCs with the exception that the bifurcation law is replaced by one that distributes the PPs into the outflow vessels with a probability weighted in proportion to the ratio of volumetric flow rates. On average, this leads to an RBC flux at bifurcations which is proportional to the respective blood flow rates. Obrist et al. (2010) showed that, in this case, the resulting mean hematocrit distribution across the capillary network remains homogeneous.

Comparing results with PPs to results obtained with RBCs will enable us to isolate the effects of the heterogeneous RBC distribution due to the network topology while maintaining correct pressure distributions and filtration metrics.

2.1.5 Time stepping

To reduce the number of required numerical solutions to eq. (6), and to remove the dependence on

the number of RBCs in the particle system, we mimic the approach of Schmid et al. (2017), and use a constant time step, Δt, to move all the RBCs in the network a corresponding arc length, $\Delta s = u_{\mathrm{rbc}}\Delta t$, along each capillary before solving the system to recover the corrected flow rates. The time step is computed for an empty network so that $\Delta t = 1/3 \min_j(l_j/u_j)$ (over all nodes j), with the factor $1/3$ chosen to increase the number of steps on the fastest edge (see also appendix A.4). RBCs and PPs that overshoot the end of their given capillary are appended to 'reservoirs' at the capillary's endpoint from which they are redistributed into the out-flowing vessels. This redistribution is performed according to a sequence of rules that apply the bifurcation law, and check that there is enough space in the branching vessel.

We should emphasise that this scheme is not time-accurate, since the flow is not updated at every bifurcation event. Our scheme does, however, ensure predictable runtimes with fixed time steps and fixed numbers of linear solves. For this reason, this choice is preferred, especially for future large-scale deployments of the code on supercomputer clusters, where reliable estimates of runtimes are essential.

2.2 Network performance metrics

Estimates of glomerular filtration rates (GFR) are the natural metric for categorising and analysing network performance in a quantitative manner. The canonical description of fluid exchange through a capillary wall is the Starling equation (Woodcock and Woodcock (2012); Starling (1896)). The filtrate volume flux can be written as

$$J_v = L_p S\left([p_c - p_B] - \sigma[\pi_p - \pi_s]\right), \qquad (8)$$

with L_p the hydraulic conductivity of the membrane, S the surface area of the filtration surface, p_c and p_B are the hydrostatic pressures in the capillary and the Bowman's capsule, respectively, π_p and π_s the plasma protein and subglycocalyx oncotic pressures respectively, and with $0 \leq \sigma \leq 1$ the Staverman's reflection coefficient. The second term in eq. (8) modulates the permeability of the membrane, with values of σ close to unity representing a membrane that is more impermeable to the solute, as is the case in the glomerulus.

In capillaries with single-file flow of RBCs the portion of the capillary surface which is exposed to the plasma is reduced to $(1-H_T)S_v$ where S_v is the full vessel surface area. As our goal is to evaluate the primary effects of the RBC distributions on the hydrodynamic component of filtration, in this study we will neglect the osmotic effects, in the terms of eq. (8) multiplied by σ. In reality, the capillary membrane is partially permeable to proteins in the solute and so the second term of eq. (8) regulates the filtration rate, with protein concentrations in the plasma varying between the afferent and efferent nodes of the glomerulus. Further to this, the fraction of the fluid filtered by the glomerulus is approximately 18%, and so the mass loss across the capillary tuft is significant (e.g. Feher (2017)).

We further assume that p_B is constant in the entirety of the Bowman's capsule and that the hydraulic conductivity L_P is also constant throughout the glomerulus. If we rewrite the capillary pressure $p_c = p_B + \delta p$, with δp, we can define the metric $\Phi_j = K_j/L_p = S_{v,j}(1 - H_{T,j})\delta p_j$ as a surrogate to quantify the filtration rate for the single vessel j. For the full network we thus define the *filtration rate* metric as

$$\overline{\Phi} = \overline{\sum_j S_{v,j}(1 - H_{T,j})\delta p_j}, \qquad (9)$$

with δp_j representing the capillary pressure perturbation which is given here as the mean of the two adjacent nodal pressures. The overline $\overline{(\,)}$ indicates that the values are averaged in time over a period of 20 s ($\approx 27\tau$).

As discussed in section 2.1.2, the presence of RBCs in the glomerular network either changes the flow rate or increases the pressure, depending on the boundary condition in use. To eliminate the effect of an elevated inlet pressure on the filtration metric, we introduce a *filtration efficiency* measure which normalises the network rate by the mean input power $\overline{P_{\mathrm{in}}} = \overline{p_{\mathrm{in}} Q_{\mathrm{in}}}$:

$$\overline{\phi} = \overline{\Phi}/\overline{P_{\mathrm{in}}}. \qquad (10)$$

Further comments on the assumptions and simplifications made to this network metric model are in appendix C.

2.3 Glomerulus geometry

With this work primarily focused on establishing the methodology for the extraction, flow simulation, and the subsequent analysis of glomeruli capillary networks, we limit ourselves to considering a subset of eleven glomeruli (as in fig. 1d), which we use as a test set in preparation for future large-scale analysis.

Glomerular geometries were obtained from the NCCR Kidney (HR-Kidney) dataset (Kuo et al. (2023)), which provides synchrotron X-ray phase-contrast microtomography of whole mouse kidneys at an isotropic voxel spacing of 1.625 µm, together with vascular and glomerular segmentations. The glomerular regions were used to extract local vascular volumes containing individual glomeruli and adjoining vessels.

The local-thickness transform follows the largest-inscribed-ball formulation of Hildebrand and Rüegsegger (1997), in which thickness at a point is the diameter of the largest ball wholly contained in the foreground and containing that point. To suppress spurious branches, this smoother thickness field was used to determine a local threshold for the signed Euclidean distance transform ϕ before thinning.

Homotopic thinning of this thresholded foreground produced a graph approximating the vessel centrelines while preserving its topology, providing a medial-axis representation. The signed distance from the original vessel surface was sampled at each vertex and stored with its coordinates, with negative values inside the vessels. For this graph representation, vessel radius was approximated by $|\phi|$ and diameter by $2|\phi|$. Coordinates and distances were stored in voxel units, with conversion to physical units using the voxel spacing.

The skeletonised, segmented glomeruli go through several pre-processing steps prior to the application of the flow solver. This is done to reduce node and edge counts – to reduce the dimensions of eq. (6) – and to remove long inlet and outlet segments connecting to the main component. These pre-processing steps are performed using the `networkx` package (Hagberg et al. (2008)), in a sequence of steps described in appendix B.

Table 1 Parameters for numerical simulations of glomeruli in this study.

Simulation time	$t = 20$ (i.e. $> 27\tau$)
mean RBC volume	$V_{\mathrm{RBC}} = 55\,\mathrm{fl}$
mean network hematocrit	$H_T = 0.25$
plasma viscosity	$\mu = 1.5\,\mathrm{mPa \cdot s}$
Boundary conditions	$P_{\mathrm{out}} = 0\,\mathrm{Pa}$
	$Q_{\mathrm{in}} = u_{\mathrm{in}} \cdot r_{\mathrm{in}}^2 \cdot \pi$
with	$u_{\mathrm{in}} = 1\,\mathrm{mm/s}$

2.4 Validation

Validation cases that capture the real-world complexity of the three-dimensional networks analysed in this paper are rare and so this code is validated against numerical simulations and experiments in simplified geometries, the details of which are summarised in appendix A.

3 Results and Discussion

The results and discussion section has two parts. The first considers the glomerulus networks from a purely topological perspective, providing a link to prior work by Wahl et al. (1984, 2004) and Terasaki et al. (2020), who considered this as a network-theory problem. The second part augments this analysis by considering fluid flow, linking shortest paths to optimal flow paths and RBC network transit times, and studying the resulting network filtration rate and efficiency.

To harmonise our discussion, and to simplify the terminology, we will refer to the more abstract 'edges' and 'nodes' in preference to 'vessels' or 'capillaries' and 'bifurcation' or 'branch' points, respectively, as we have done up until this point. Our reason for making this choice is best illustrated by an example. If we have a large-diameter vessel, AA', with a small-diameter daughter vessel, BB', attached at point B to AA', attempting to characterise whether AA' is or is not a single continuous vessel consistently becomes difficult. Instead, we will adopt the convention that AA' is formed of two separate *edges*: AB and BA', the endpoints of which are the *nodes* A, B and A'.

Unless otherwise stated, the key parameters for all simulations presented in this paper are as described in table 1, and the network properties for the 11 cases considered in this work are displayed in fig. 1.

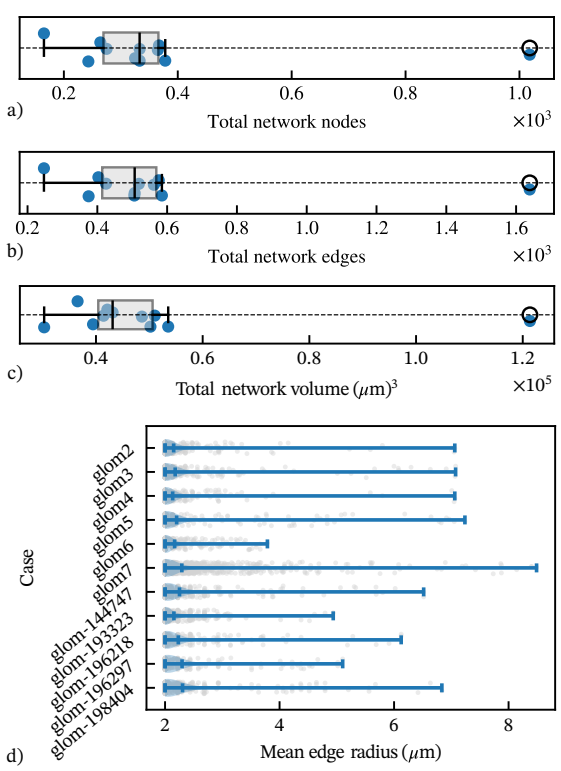

Fig. 1 The key values of the 11 glomerular networks analysed in this study. Total network values are shown for a) the number of nodes, b) the number of edges and c) the volume. Mean edge radii and plotted for each network in d).

3.1 Network topology and shortest paths

We begin our analysis by considering the number of edges in the path between the inlet and outlet ends of the glomerular tuft. The traditional analysis by Wahl et al. (2004), Terasaki et al. (2020) and others, has been to consider the shortest path defined as the path with the minimum number of edges between inlet and outlet. Figure 2a shows that these paths typically comprise between 10 and 20 edges, and appear uncorrelated with respect to the total number of edges in the graph. These results are in agreement with earlier observations (Wahl et al. (2004); Terasaki et al. (2020)), but it is worth noting that our results show a greater variability than the results by Terasaki et al. (2020), and an overall longer path length, although their networks were smaller (node counts ranging from approximately 75 to 250 nodes),

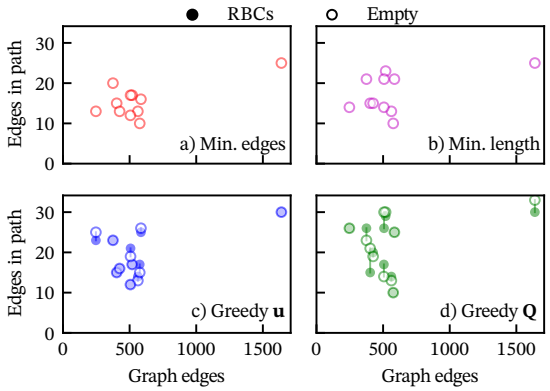

Fig. 2 The lengths of the shortest paths based on different metrics. Results in panels c) and d) were obtained using a flow field computed with RBCs (filled symbols) and alternatively without RBCs (empty symbols).

whereas in this study the node count ranges from 165 to 1018.

Instead of counting the number of edges, one can alternatively consider shortest paths with respect to the total edge length (fig. 2b). This becomes particularly relevant in cases where networks undergo many bifurcations over short length scales, where a path with more edges but an overall shorter length, might present a more optimal path for fluid and RBC transport. Results show that the maximum shortest path length has increased to 23 edges, while the minimum remains unchanged. The total path length also remains uncorrelated with respect to graph size.

As a third option, we add information about the flow into the graph, and we define the **u** *greedy path* of an RBC by choosing the path which follows the highest flow velocity at each node. The difference between this and the topologically shortest path is that we now follow a hypothetical particle that is subject to the same bifurcation behaviour at the nodes, and we account for the flow direction on each edge, which may not necessarily be aligned with the path direction when considering the minimum edge and minimum length paths. Computing these greedy **u** paths and plotting the number of edges per path in fig. 2c shows shortest path lengths varying from 12 to 30 edges. Except for a few cases, these are longer than the two corresponding categories of topological path, and hence indicate that different paths are being selected, however the lack of correlation with increasing graph size suggests that at least some of

the conclusions reached by Terasaki et al. (2020) translate also to the hydrodynamic properties of these networks, despite these paths diverging.

In addition to computing these paths for empty networks filled with plasma, time averaged hydrodynamic solutions of the network with RBCs showed the greedy path changing in five of the eleven cases considered, though only up to a maximum of 2 edges, suggesting a degree of robustness in this measure, though edge capacity and availability of accommodating the RBC on the edge is not taken into account when computing the path.

While the ZF-effect is determined by flow velocity ratios at the nodes, direct simulations of plasma with RBCs demonstrate the saturation of some high velocity branches. This then causes either a velocity drop or an alternative bifurcation, and leads to a greater flux of RBCs along alternative pathways to those found using the greedy **u** path analysis. This effect is most often observed at nodes where the edges bifurcate into a high-capacity, slow and wide edge, and into a low-capacity, narrower but faster edge. In this case the fast edge quickly saturates, and the majority of RBCs traverse the slower branch. To account for this, the greedy path is modified to consider instead the volumetric flux **Q** at the nodes, with the results plotted in fig. 2d. As in the previous results, there is no clear correlation between shortest path length and network size.

Comparing the shortest path lengths for networks with and without RBCs (filled and empty symbols in fig. 2c,d), we observe that the shortest path lengths with the greedy-**Q** criterion are more sensitive to the presence of RBCs that the greedy **u** paths.

Although the different criteria for identifying the shortest paths may not define the exact same path, the qualitative consistency between the four results shown in fig. 2 suggests that there exist more optimal transport paths in the glomerulus, even though it may not be the topologically optimal route. To emphasise this further, fig. 3 shows three examples of glomeruli from this study: one where all four paths align (*glom3*) and the other two (*glom2* and *glom5*) each of which have four distinct paths.

3.2 Sensitivity of shortest paths

Results in fig. 2 and fig. 3 do not account for any uncertainties in the edge diameters that arise in the segmentation of the glomerular network from the raw image data. To assess the sensitivity of the four paths to such uncertainties, we select a single glomerulus (*glom2*) as a test network. With the mean edge diameters defined through the diameters at the endpoints, these are modified by random perturbations of the form $d_0 + \alpha\psi$, where ψ is a uniformly distributed random variable over the interval $[-1, 1]$, and $\alpha = 1.625\,\mu\text{m}$ is the amplitude corresponding to the isometric voxel size of the image data. In all cases, we ensure that no vessels have a diameter smaller than $4\,\mu\text{m}$. Any vessels that are, are set to have a diameter of $4\,\mu\text{m}$.

A total of $20,727$ perturbed networks are generated, with the edge radius statistics summarised in fig. 4. The minimum diameter threshold applied to the narrowest edges results in a non-zero mean deviation in the smallest capillaries.

It is clear that, from a graph topology perspective, the applied perturbation vector does not affect the minimum edge and minimum length-based paths, which we previously defined and computed in fig. 2 and fig. 3, and for this reason we exclude them from consideration. Although not presented here, the same paths computed on directed graphs, which take into account flow direction, were also entirely insensitive to the perturbation, as there was no flow reversal along the traversed pathways. The two forms of a greedy shortest path, however, are directly affected by the flow velocities and are therefore shown in fig. 5 in the form of histograms that group the shortest paths by the number of edges, with the bar heights normalised by the total number of perturbed networks. Red dashed lines indicate the values for the unperturbed network.

Whereas the shortest path lengths for the greedy-**u** criterion are quite robust, the shortest path length for greedy **Q** without RBCs is more sensitive and exhibits a bi-modal distribution, with an initial set of paths between $17 - 18$ edges in length, followed by a second subset of paths with $26 - 30$ edges. Sensitivity characteristics of the empty and PP-perfused networks are similar, with near-identical distributions, which is expected given that PPs are distributed equally

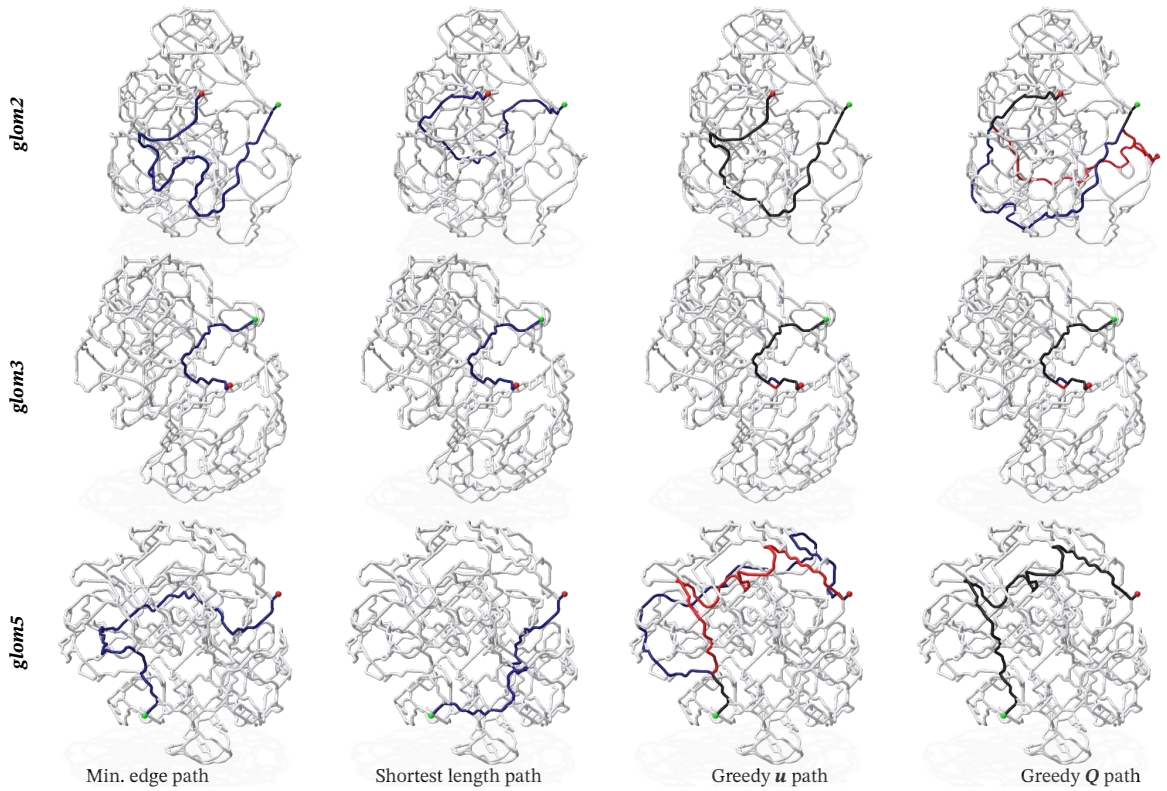

Fig. 3 The four shortest paths for 'glom2', 'glom3' and 'glom5'. Blue and red traces for the two sets of greedy paths indicate the paths chosen within empty and RBC-filled network mean flow fields.

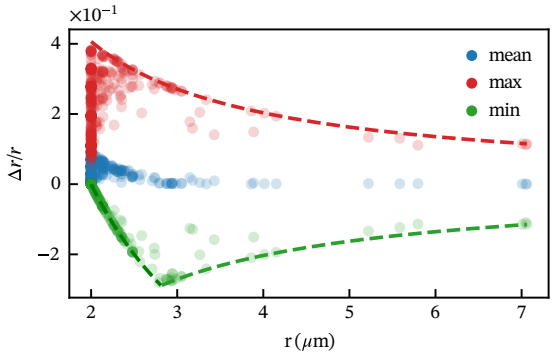

Fig. 4 Edge radius perturbation statistics. Mean, minimum and maximum radii for each edge are reported by blue, green and red markers, while theoretical extremal values are given by dashed lines.

throughout the network and thus, for a given perturbed network, the flow ratios are expected to remain the same at nodes. These are also the most sensitive, with more than 50% of the cases resulting in paths much shorter than the unperturbed case. RBC-perfused networks, however, were observed to be more stable with respect to the shortest path length, which can be seen as another example of the stabilizing effect of RBCs in microvascular networks described by Schmid et al. (2019).

3.3 RBC trajectories and transit times

To extend the study of shortest paths, we track the distribution of RBCs in evolving flow fields taking into account the global coupling between RBC distribution and plasma flow. Three primary metrics are considered: the instantaneous RBC distribution in the network, the RBC transit times and the paths of these particles for a given range of transit times.

Figure 6 shows snapshots of the RBC locations for three networks after the initial transients have passed and a statistically stable configuration has

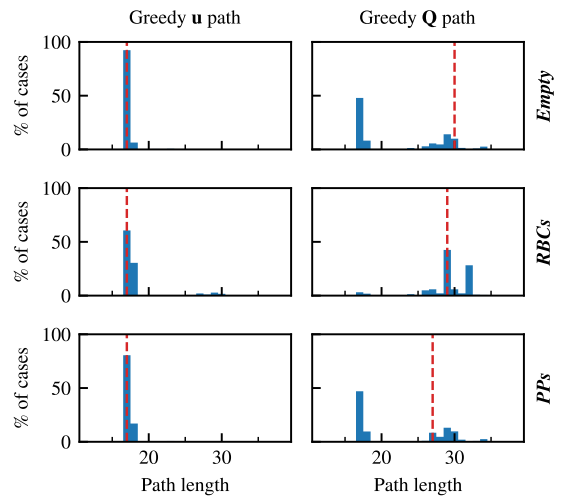

Fig. 5 Histogram of shortest paths statistics for the randomly perturbed *glom2* network. Bifurcation paths are unaffected. Most sensitivity observed for the two forms of greedy path. Paths computed for flows with RBCs are most sensitive due self regulation. The red dashed lines denote the path length in the unperturbed case.

been reached ($t > 15\,\mathrm{s}$ or $t \gtrsim 20\tau$). The colour of each RBC indicates the time since the RBC entered the network. The networks are partitioned into a high hematocrit region and low hematocrit region, as is especially evident in the *glom2* and *glom3* networks. In the *glom5* the partitioning is less strong and the low hematocrit region is populated with older (and, thus, slower) RBCs. Moreover, all cases indicate a clear 'fast' path between the inlet and outlet (darker RBCs). However, this fast path is not the exclusive trajectory for RBCs, and instead the fast path is embedded in the high hematocrit region of the network. Our earlier discussion in section 3.1 and fig. 3 indicated some degree of sensitivity in the shortest paths, firstly with respect to the metric chosen to compute it and secondly with respect to the flow field, so it is perhaps not surprising that RBCs would distributed in the vicinity of the fastest path.

The RBC transit times are presented in fig. 7 as a histogram, scaled into a probability density function. Peaks and features of interest in these histograms are highlighted for given transit-time intervals and the corresponding tracks are plotted in fig. 8 for both RBCs and PPs. The histograms of all networks follow a broadly similar pattern. First, there is a sharp, well-defined peak representing the fastest possible transit times through the network with limited variation in transit times due to the limited fluctuations of the flow velocities along the fastest path. This sharp peak is sometimes followed by small, but still well-defined (see e.g. the blue and green intervals in the histograms for *glom2*) while the longest transit times form a broad peak with a long decaying tail as t/τ increases. In fig. 7 we show histograms only to the upper limit $t/\tau = 4$. In all but 2 of the 11 cases considered, this limit captures 95% of the RBCs. More than 50% of the RBCs captured within $0 \leq t/\tau \leq 1$ in all cases.

Since PPs propagate diffusively, they take a larger range of possible paths through the network. We expected this to lead to a significant broadening of the peaks in the histogram when compared to RBCs. This proved not to be the case. Instead, the histograms for both RBCs and PPs reflect the flow state within the network, and thus serve as a signature of the global topology that ultimately determines the macroscopic flow structure.

With this in mind, and despite our limited subset of cases, we try to identify two distinct classes of glomeruli. These are: glomeruli dominated by the fast transit time dynamics, such as *glom3* in fig. 7, and glomeruli in which the majority of the transits occur in the broad, slow peak of the corresponding histogram. Of these, the former are easiest to explain. These are networks that have a shortcut between inlet and outlet, with large capacity and/or high volumetric flow rate, which we deduce from the dominance of the fast peak in the PP transit data. The flux of PPs is highest on edges with high volume flux, and the low variance indicates a common path, further confirmed by the particle track visualisations in fig. 8 which correlate the peaks to the particle paths.

The other class of glomeruli still retains the peak corresponding to the fast pathway, but now a significant portion of the transport occurs through peripheral areas of the network, through more complex and diffuse paths, as seen in the case of *glom2* and *glom5* in fig. 8. In the periphery, the capillaries are narrower and each is of approximately similar size, so both RBCs and PPs have a greater number of possible paths that can be taken between the inlet and outlets, leading to a greater spread of transit times. Diversion of RBCs

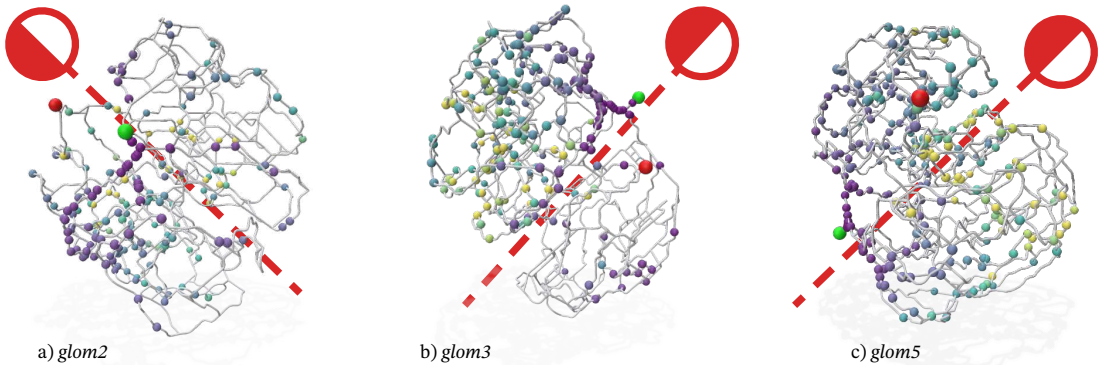

Fig. 6 Subset of three glomeruli with RBCs positions indicated. The colour denotes the time elapsed since the RBC entered through the inlet (darker/purple is younger, lighter/yellow is older). The glomerulus is clearly separated into two lobes, with one highly perfused while the other is left relatively empty, as indicated by the red semi-circle. Inlet and outlet nodes are shown in green and red markers, respectively.

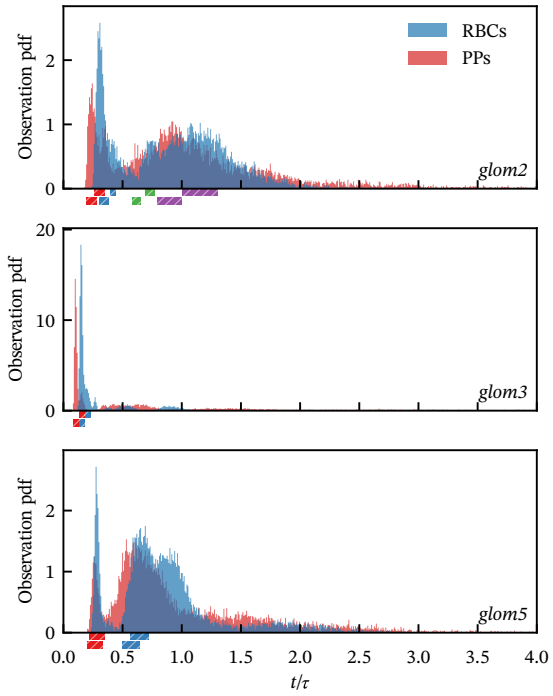

Fig. 7 Histograms of RBCs and PPs in a subset of three networks. Coloured intervals underneath the x-axis of each plot correspond to the paths visualised in fig. 8, the transit times of which fall within each time range.

away from the fastest path into the periphery, due to altered network flow rate balances and capacity constraints, results in networks attaining this diffusive characteristic in transit times.

A detailed investigation into the reasons why these networks fall into these two classes is a topic for further study and requires larger datasets to draw the appropriate conclusions.

3.4 Network performance and efficiency

Figure 9 shows histograms of the ratios of overall network performance for all glomerulus networks perfused with RBCs versus PPs, as measured by the mean filtration rate $\overline{\Phi}$ and them mean filtration efficiency $\overline{\phi}$. For all glomeruli we observe $\overline{\Phi}^{\mathrm{RBC}} > \overline{\Phi}^{\mathrm{PP}}$, with a maximum gain of over 16%. Normalisation with respect to inlet mechanical power showed that eight of the eleven glomeruli had an increased filtration efficiency $\overline{\phi}$ when perfused by RBCs, with maximum efficiency gains on the order of 5%. These results suggest that a heterogeneous distribution of RBCs is indeed beneficial for glomerular efficiency, and that the specific network topology with distinct shortest pathways is an important element in this effect.

The observation that the increase in filtration rate $\overline{\Phi}$ is higher than the increase in filtration efficiency $\overline{\phi}$ is mostly due to higher inlet perfusion pressures with RBCs.

This indicates that the heterogeneous distribution of RBCs generally leads to a higher overall network resistance (compared to a homogeneous distribution). As we have seen previously, the fastest paths are often saturated by RBCs, often resulting in longer transit times when

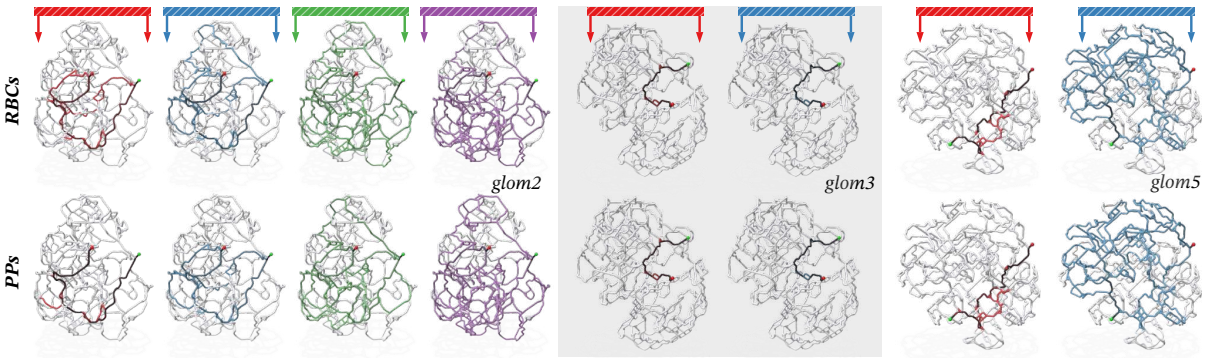

Fig. 8 Transit paths of active and passive particles for given transit durations. The coloured bars above the networks correspond to the time ranges under the x-axis of fig. 7. The pathways become more diffused with increasing transit times.

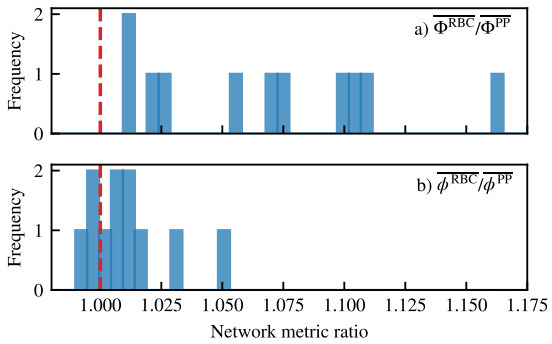

Fig. 9 Network metric ratios with RBCs and PPs. Panel a) considers the raw values, while panel b) normalises these against the applied power to the system $p_{\text{in}}Q_{\text{in}}$, to remove the effect of changing inlet pressure.

compared to PPs. The saturation of this pathway increases the hydraulic resistance within the glomerulus. In addition, this forces more flow to pass through peripheral areas of the network, which have smaller capillary diameters. This extra resistance is counterbalanced by low tube hematocrits in these peripheral areas and leads, at least in this small subset, to an increase in efficiency regardless.

We now extend our analysis of filtration performance by assessing the robustness of the results presented in fig. 9. To this end, we measure filtration rate and efficiency for the large ensemble of perturbed networks already used for the sensitivity study of shortest paths (section section 3.2).

The histograms in fig. 10a show $\overline{\Phi}$ for the perturbed networks. We find that the unperturbed cases (dashed lines) are mostly overestimating the filtration rates. We also note that the introduction of particles (RBCs or PPs) generally increases the filtration rate which can be attributed to the elevated pressures at the inlet necessary for transporting the particles through the network. Pairwise comparisons between empty, RBC and PP-perfused cases (Figure 10b) illustrate that the respective mean filtration rates $\overline{\Phi}$ are highly correlated, and that filtration rates are consistently higher in the networks with RBCs than in the networks perfused with PPs. Statistical testing of pairwise samples with the Wilcoxon signed-rank test shows that the increase in $\overline{\Phi}$ when moving from PPs to RBCs is statistically significant ($p < 0.01$).

Figure 10c,d show the corresponding data for the mean filtration efficiency $\overline{\phi}$, i.e., mean filtration rate normalized by mean input power. In contrast to the results for the filtration rate, we see that the efficiency drops when particles are added. This is expected as the transport of RBCs (independent of their distribution in the network) strongly raises the network resistance and the required input power. At the same time, we observe that the RBCs yield slightly more filtration efficiency than the PPs. Although the difference is smaller than for the mean filtration rate, we find that the increase in filtration efficiency for RBCs vs. PPs is statistically significant ($p < 0.01$, Wilcoxon signed-rank test).

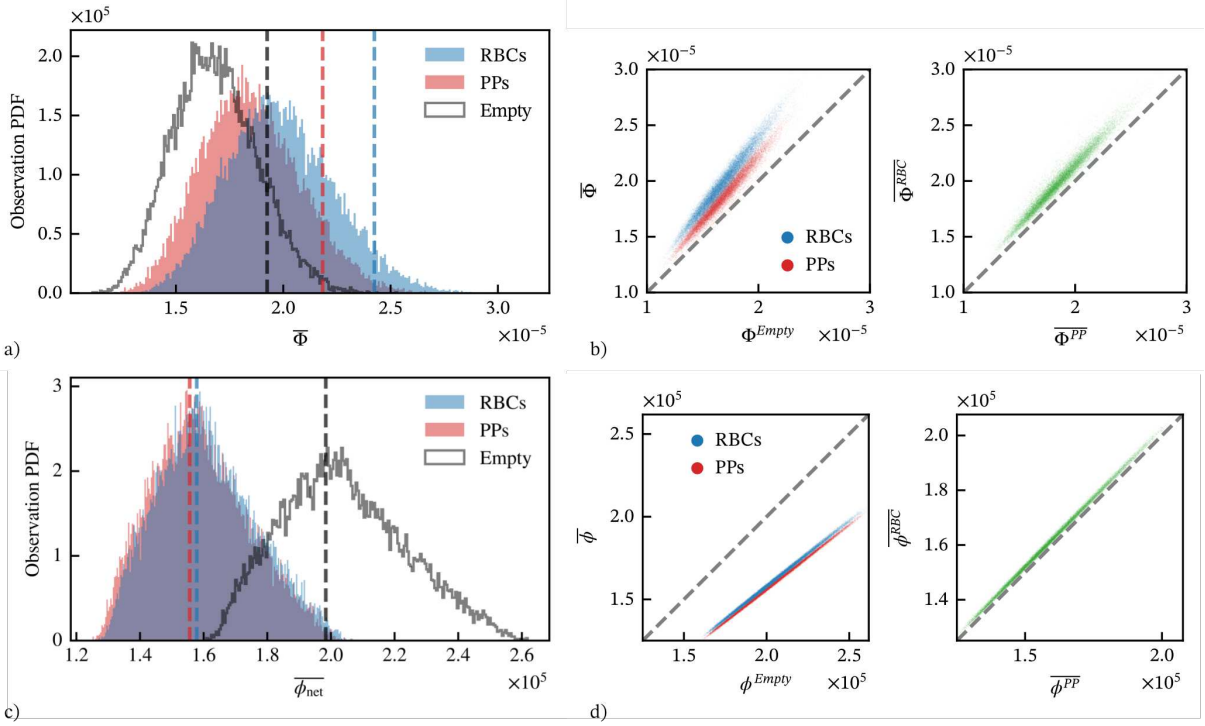

Fig. 10 Total network metric sensitivity analysis for 20,727 randomly perturbed samples of the 'glom2' network: a) Histograms of the network metric, Φ for empty, RBC- and PP-perfused networks, shown alongside the values for the unperturbed network in the dashed lines. b) Correlations of Φ between the RBC-, PP-perfused and empty networks. c,d) Corresponding plots showing the power-normalised efficiency metric ϕ.

4 Summary and future outlook

In this paper, we have developed a methodology to test the hypothesis that the combination the network topology and the ZF-effect affect the filtration of blood in the glomerulus.

For this, 11 glomeruli were extracted from the NCCR Kidney dataset to obtain initial observations and adapt the analysis methodology to the eventual extension of the analysis to the complete dataset.

Building upon earlier work, this study first confirms prior observations, that the shortest paths by the number of edges between the afferent and efferent ends of the network are invariant with respect to network size, for the 11 examples considered. This was then extended, first to look at shortest paths based on traversal distance, and then on to two new pathways that were defined by as the path taken by a model particle following the fastest outflow velocity or largest volumetric flow rate at each node, respectively. The distance, local-flow-velocity-based and volumetric-flow-rate-based paths were also observed to be independent of network size, albeit with a greater range of path lengths. In most cases the four kinds of path diverged in their exact routing, suggesting that the *shortest path* is perhaps not an intrinsically fixed property of the network.

A sensitivity analysis that considered small variations in edge radii for one of the glomeruli showed that, while the greedy velocity-based path was reasonably robust in all cases, the volumetric-based pathways were more sensitive in the absence of the ZF-effect compared to networks perfused by RBCs.

Simulations of the RBC dynamics within the networks showed a clear concentration of RBCs in the region of the shortest paths. Furthermore, transit time histograms, computed from individual particles moving through the networks, were seen to function as signatures for the underlying topology, with two distinct classes of networks

observed. These two classes represent networks dominated by transport along the fastest path and those where RBC transport occurs predominantly along more circuitous pathways in peripheral areas of the glomerulus.

Filtration rate was seen to increase in all 11 networks in the presence RBCs under the influence of the ZF-effect compared to passive particles, mostly due to increased inlet pressure resulting from increased resistance in the network with RBCs. Filtration efficiency gains were more modest, with 8 of 11 networks seeing an improvement, and a maximum efficiency gain of 5%. Sensitivity analyses demonstrated that the observed increase in filtration rate and efficiency are robust with respect to uncertainties in edge diameters. This result supports the hypothesis of this study that hematocrit heterogeneity in the glomerular network, in association with the specific topology of the glomerular networks, leads to enhanced filtration.

With the methodology and approach established in this study, there is now scope for future work to apply these methods to larger collections of skeletonised glomeruli available through the NCCR Kidney dataset. The glomeruli identified there are in-situ within the rest of the renal vasculature, and therefore it is possible to correlate properties of the network topology and function with the location within the renal cortex.

Further improvements could also be made by introducing more advanced filtration and blood plasma models which account for time varying plasma protein and solute concentrations, and modelled mass loss through the capillary walls. Ideally this should be combined with corrected models for the effect endothelial surface layer on flow resistance that are specific to the properties of the glomerular capillaries, to enable these results to be correlated directly with experimental observations.

Supplementary information. The three-dimensional structures of the glomeruli are visualised using Polyscope (Sharp et al., 2019).

Acknowledgements. The authors would like to thank Michael S. Goligorsky for our many fruitful discussions with him and for his comments and suggestions throughout this project. We would also like thank Willy Kuo and Vartan Kurtcuoglu for our discussions relating to the NCCR Kidney project.

Table A1 Parameters for the hexagonal lattice validation case.

Case description	Hexagonal lattice
Type	Numerical
Edge section	Circular
Edge dimensions	$d = 7\,\mu\text{m} + \delta d$
Edge length	$60\,\mu\text{m}$
RBC volume	56.51 fl (rat)
Network H_t	0.4
Fluid viscosity	$\mu = 1.5\,\text{mPa} \cdot \text{s}$
Boundary conditions	Flow rate $q_{\text{in}} = 50\,\mu\text{m}^3/\text{ms}$

Declarations

Funding. Funding for this project was provided by the King Abdullah University of Science and Technology as part of a postdoctoral fellowship.

Conflict of interest. The authors declare no conflicts of interest.

Author contributions.

- Conceptualization, methodology, project administration: Anton Glazkov, Dominik Obrist, Peter Schmid;
- Data curation: Anton Glazkov, Diego Rossinelli;
- Formal analysis, investigation, software, validation, visualisation and writing - original draft preparation: Anton Glazkov;
- Funding acquisition and resources: Peter Schmid;
- Supervision: Dominik Obrist, Peter Schmid;
- Writing - review and editing: Anton Glazkov, Peter Schmid, Dominik Obrist, Diego Rossinelli;

Data availability. This project uses publicly available data, as part the NCCR Kidney (HR-Kidney) dataset available at the Image Data Resource (IDR) repository at https://doi.org/10.17867/10000188. For further details, see Kuo et al. (2023).

Materials availability. Not applicable.

Code availability. Not applicable.

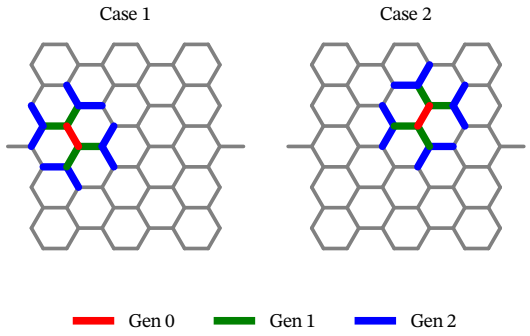

Fig. A1 The hexagonal lattice validation case. The perturbation is applied to the central part of the 'Gen 0' edge in each case, as described in the text. Resulting flow changes are monitored the all the labelled regions. Flow direction through the network is left to right.

Appendix A Validations

A.1 Hexagonal capillary bed

The geometry under consideration is a hexagonal lattice with symmetrically placed inlow/outflow edges and a left-to-right flow through the network, described by the parameters summarised in table A1, and fully detailed in Schmid et al. (2015).

This study investigated the presence of a self-regulation mechanism that arises due to the stabilising properties of the phase separation effect. In addition to the base network, two sub-cases are considered here that compare changes in the flow field due to the dilation of two edges in two separate parts of the network. The dilation consists of a 15% increase in the central 48 µm section of the target edges, shown in fig. A1 and by the red edges in fig. A1, with the effect on the flow measured in the labelled regions. To match the geometry, the perturbed edges are modelled as chains of three edges, and the code run without the edge simplification procedure detailed in the main text, so as to maintain the same diameter at all nodes with three edges.

Mean flow values are obtained by removing transients for $100\tau_{\text{net}}$ following which the flow is averaged in time over $1000\tau_{\text{net}}$, where τ_{net} is the network turnover time, with respect to the volumetric flow rate at the inlet.

Mean edge RBC counts are shown in fig. A2 for the unperturbed flow case. The distribution

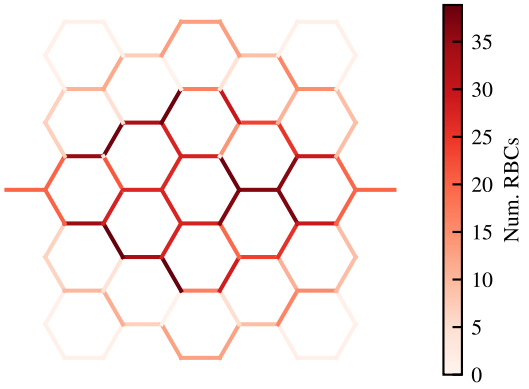

Fig. A2 Mean edge RBC counts for unperturbed lattice.

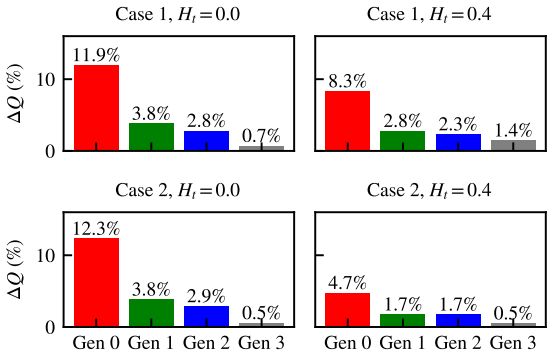

Fig. A3 Relative change in flow rates due to case 1 and case 2 edge dilations.

matches corresponds well with observed values in Schmid et al. (2015) both in number and overall global distribution.

Figure A3 demonstrates the mean tube hematocrit changes between the perturbed and unperturbed flow solutions for the edges labelled in fig. A1. These changes match well with observed flow changes in the earlier work, with the flow regulation effect of RBCs clearly established. Volumetric flow rate changes in the $H_T = 0$ system match exactly in all but the 'Gen 1' branches, possibly due to the effect of endothelial cell layer, which is modelled in the literature but not in the present model. In the $H_T = 0.4$ system, a stabilisation of the flow rates is observed, alongside an increase in the ΔQ from 0.7% to 1.5% in the peripheral parts of the net, in the 'gen 3' branches, which is characteristic of the flow in this case. We

Table A2 Parameters for rectangular lattice validation case.

Case description	Rectangular lattice
Type	Numerical
Edge section	Circular
Edge dimensions	$D = 5\,\mu\text{m}$
Edge length	$50\,\mu\text{m}$
RBC volume	157.0 fl (arbitrary)
Network H_T	0.4 / 550 particles
Fluid viscosity	$\mu = 1.5\,\text{mPa}\cdot\text{s}$
Boundary conditions	Flow velocity $u_{\text{in}} = 1\,\text{mm/s}$

Table A3 Parameters for ladder network validation case.

Case description	Ladder capillary
Type	Experimental
Edge section	Rectangle
Edge dimensions	$w =, h = 10\,\mu\text{m}$
Edge length	*variable*
RBC volume	94.1 fl (human)
Network H_T	0.10
Fluid viscosity	$\mu = 1.5\,\text{mPa}\cdot\text{s}$
Boundary conditions	Flow velocity $u_{\text{in}} = 1\,\text{mm/s}$

should note that the observed increases in the flow rates within the 'Gen 0' branches are higher than those in the reference model. We again attribute these to the effect of the cell layer.

Overall the results from this validation case demonstrate that the numerical model in this paper is able to capture the mean spatial distribution of the RBCs within the network, accurately predicts the flow rates and the response of the flow to edge thickness perturbations, and captures the key physical self-regulation effect, which is critical for capturing an accurate description of the RBC dynamics in an arbitrary network.

A.2 Rectangular lattice

A study investigating RBC perfusion through a 10×10 square lattice was conducted numerically and described in Obrist et al. (2010). Each edge of the lattice is $50\,\mu\text{m}$, with a circular cross-sectional diameter of $5\,\mu\text{m}$. Particle sizes are determined from the quoted $8\,\mu\text{m}$ length of the confined particle, giving each particle an effective volume of approximately 157 fl, giving an average network hematocrit of $H_{\text{net}} = 0.4$ and a total of 550 particles.

In fig. A4, the results obtained from the simulations using the present code, demonstrate near identical particle distributions as in the reference literature, including a cell-depleted region in the central part of the lattice by $\tau = 1.5$, a concentration of particles near the outlet, and clustering of the large bulk of particles in the two remaining corners. A key difference between these results and those in Obrist et al. (2010) is the enforced separation of particles along the lengths of the capillaries. This necessarily limits the particle density in these corner regions and therefore smooths out the particle density gradient towards the central region of the lattice.

A.3 Ladder geometry

The ladder geometry of Hyakutake et al. (2023) represents a capillary at the periphery of a tissue. That is, two parallel capillaries are joined by six perpendicular edges in between, forming a ladder-like structure. Micro-circulation experiments with this geometry have investigated the phase separation effect under different geometric parameters, such as the length between bifurcations and the relative width of the microchannels. The flow domain is summarised in fig. A5, and labelled with the associated parameters. Manufacturing these microchannels requires etching the substrate, with the result that the channels have rectangular cross-sections, which we account for in our fluid model by using the hydraulic diameter. We also modify the network pre-processing steps, described in appendix B, so that the branch B_6 is not amalgamated into one edge with the incoming parent branches.

With these modifications applied, we find that the solution for the fluid flow rates in the empty network accurately matches the reported flow rates in Hyakutake et al. (2023), once again confirming the correct implementation of our fluid model, as seen in fig. A6a.

Despite B_1 having the highest flow rate, the observed peak hematocrit distribution in the experimental results actually occurs within the second branch, B_2, contrary to the standard phase separation model of Pries used in our approach, which predicts higher hematocrit values in B_1, as seen in fig. A6b. This is explained in Hyakutake et al. (2023) by accounting for the radial

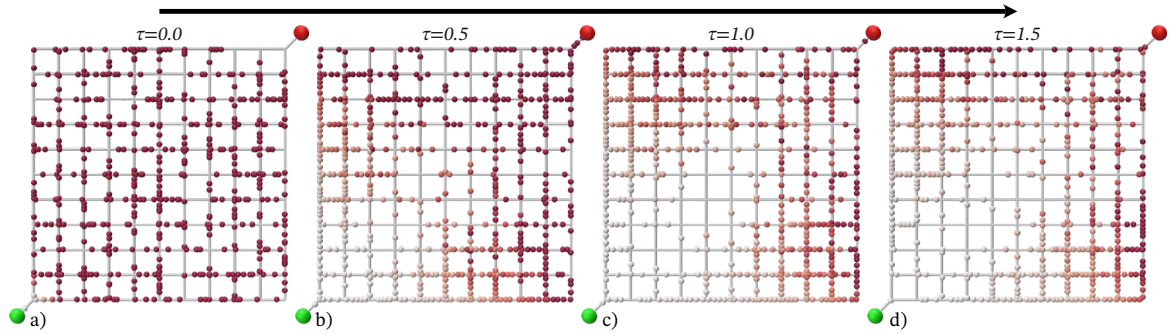

Fig. A4 The results of the validation of particle transport on a rectangular lattice from Obrist et al. (2010), showing the distribution of particles in the network at increasing time stamps.

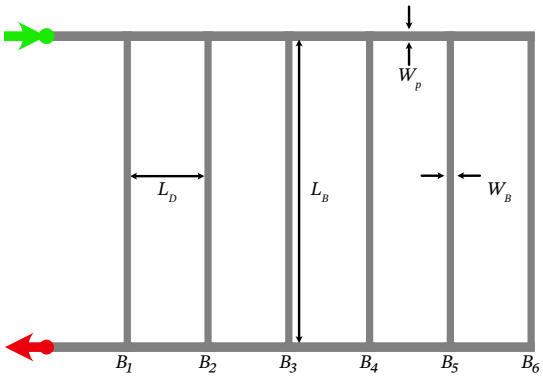

Fig. A5 The ladder network geometry. The parameters governing the flow in this network are summarised in the labels.

displacement of RBCs within the capillary. As cell-depleted plasma is skimmed off in the first branch, RBCs are sucked closer to the wall of the capillary thereby making it more likely that they will enter the second branch. The result is that observed values in our simulation, shown in fig. A6b, differ from those in the experiment, with most of the RBCs transiting through the first channel in the numerical simulations. Despite this, the numerical data shows that downstream channels are nevertheless still perfused by the RBCs. In fig. A6b, we have also included the hematocrit fractions for the PPs, which demonstrates a uniform mean hematocrit in all branches, as expected.

Furthermore, we note that the narrowest channel width used in the experiment is 10 µm, which is larger than most of the vessels diameters considered in our numerical model. In our case, the majority ($\sim$ 97%) of vessels are smaller than 10 µm, and the vertical displacement of the RBC is no longer a factor since the cell is constrained by the capillary walls. As we have mentioned before, however, the first sequence of bifurcations is the most critical in determining the global distribution of RBCs, and so these cell migration effects are likely to be observed at the first few bifurcations in the glomerulus.

A.4 Time step sensitivity

Having taken the choice to apply a computational model that is not time-accurate, a choice that we have explained and justified in detail in section 2.1.5, it is natural to consider the sensitivity of the results to changes to this global time step. This is specifically relevant for the 'fastest' edges in the network, since there is a high probability that multiple RBCs will have to be redirected into the child edges under a flow that has not been updated. It has also been shown by Merlo et al.; Hyakutake et al. (2023) that the RBC configuration in the system is highly sensitive to the phase-separation characteristics at the first few bifurcations. Although those particular studies considered the axial migration of the RBCs to the boundaries of the capillary, logically this translates to any modification to the bifurcation properties, because the initial choice often determines which portion of the network an RBC ends up in.

To quantify these sensitivities, two networks are tested. In the first case, a simple network with one bifurcation and two parallel edges with balanced flow rates is selected (see fig. A7), since the RBC dynamics here are highly sensitive at the

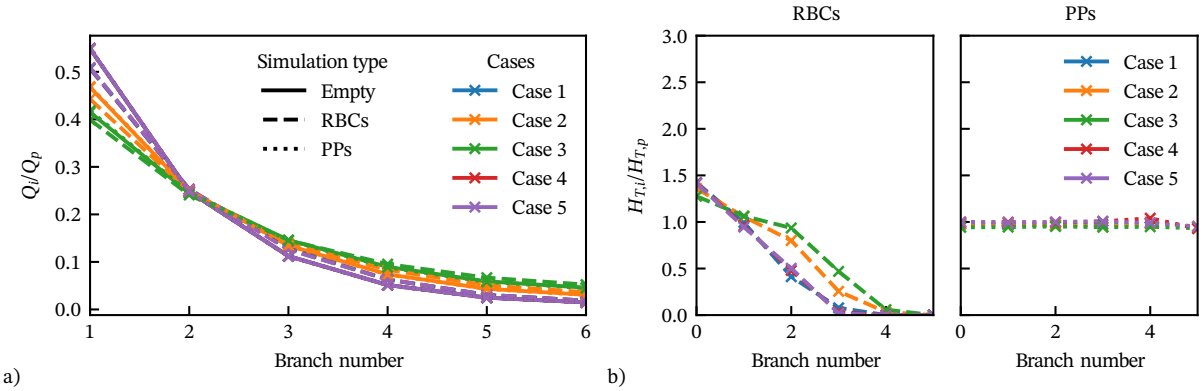

Fig. A6 The flow rate and tube hematocrit ratios for the ladder geometry. Hematocrit calculations are performed with RBCs and PPs to validate both the bifurcation model for the RBCs and the flow-rate-based particle advection of the PPs.

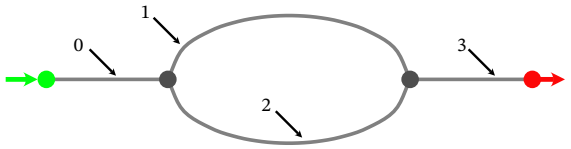

Fig. A7 The parallel-branch network used for evaluating time-step independence. All edges in this network have the same thicknesses.

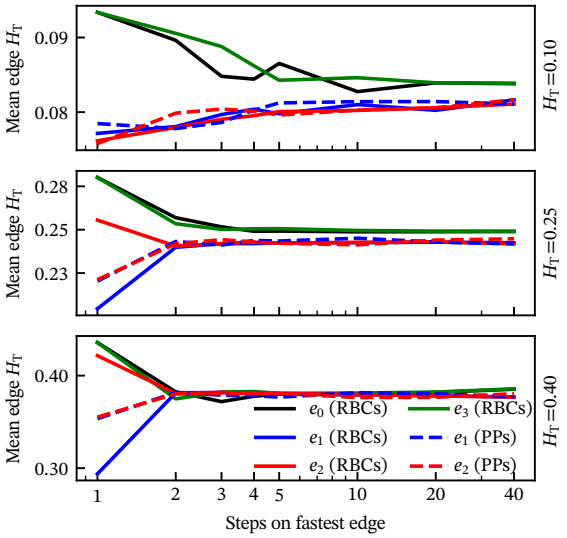

Fig. A8 The mean tube hematocrit balance in the inlet, outlet and the two parallel edges of the network in fig. A7, at network hematocits of 0.1, 0.25 and 0.4, shown for cases computed with increasingly finer time steps.

only bifurcation in the flow. The second example considers the *glom2* glomerulus, with it being typical of the networks analysed in this paper, and it is also the case considered in the edge-thickness sensitivity analysis in section 3.2 and section 3.4.

Flow parameters for these two cases are run with RBC volumes of 55 fl, and an inflow velocity of $1\,\mathrm{mms}^{-1}$ and a fluid viscosity $\mu = 1.5 \times 10^{-}3$. The parallel-edges case is run at network hematocrits of 0.1, 0.25 and 0.4, while the glomerulus network is run at a fixed hematocrit of 0.25, to match the analysis in the rest of the paper. The former case is run over $\tau = 100$ time steps to remove transients and $\tau = 500$ to time average the data, while the glomerulus network is run with $\tau = 15$ for transient removal and $\tau = 20$ for data capture.

The mean hematocrit data for the parallel-edge case in fig. A8, shows that the sensitivity of the mean hematocrit distribution is greatest for the lowest network hematocrit, requiring higher temporal resolution to stabilise the solution compared to the higher hematocrit cases with $H_T =$ 0.25 and $H_T = 0.4$. In these latter cases, increasing the number of steps on the fastest edge by 3×, or, equivalently, taking a timestep that is 1/3 the size, is enough to stabilise the solution. This effect occurs because in systems that only have a few RBCs, the influence on the mean of placing the particle into the incorrect capillary is greater, and, if these particles form *plugs*, the error might be applied consistently at every flow-through instance. On the other hand, for

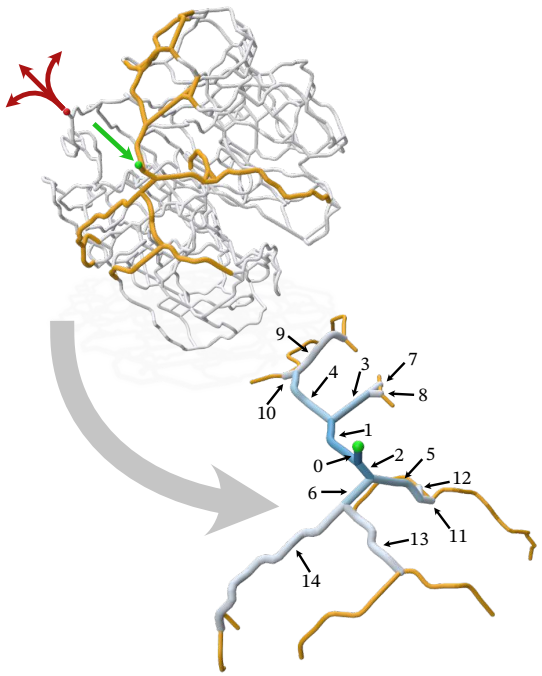

Fig. A9 The glomerular network for the glom2 case, with the inlet and outlet indicated with green and red arrows, and the first 5 generations of edges from the inlet shown by the orange sub-network. This sub-network network is isolated and the edges of the first 4 generations of edges, which are used in the timestep sensitivity analysis, are labelled and illustrated in progressively lighter shades of blue.

high-hematocrit cases, any given particle may be distributed with some error, but this error disappears in the average over multiple iterations of the system. We also observe that the sensitivity properties of the active and passive problems are similar for scale factors greater than 1, and so both problems can be advanced in time with the same algorithm and with the same time step size.

Similar results are obtained for the glomerulus, with the network topology, as well as the labelled bifurcation structure illustrated in fig. A9, where the first 4 generations of bifurcating vessels are considered in the analysis. Ratios of tube hematocrit are considered at each bifurcation, in preference to raw hematocrit values, to remove any variability in the inflow RBC flux. Changes in the hematocrit distribution also affect bifurcation behaviour by affecting the global flow, though this effect is minimised too once the flow state converges with sufficiently small timestep.

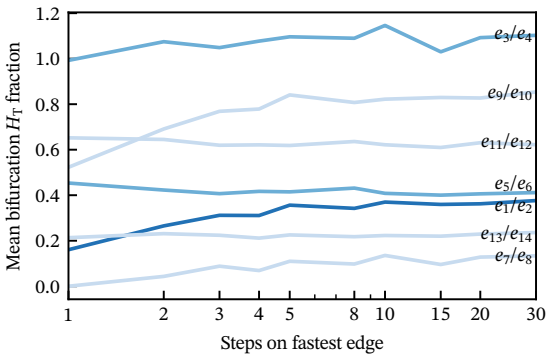

Fig. A10 Hematocrit fraction at each bifurcation in the 4-generation sub-network, as labelled in fig. A9, and coloured by generation level.

Results in fig. A10 show that the flow largely converges with 3 time steps per fastest edge, with the most sensitive being the first bifurcation and the e_9/e_{10} node. The first bifurcation is expected to be the most sensitive, but it is somewhat surprising to see additional sensitivity in the later case. A possible explanation is that at that node the flow is nearly balanced, and is therefore very sensitive to changes upstream, especially the earlier generations of edges, since the bifurcation behaviour is likely to be very highly resolved at the node connecting edges 9 and 10, due to significantly slower flow speeds there.

To conclude this analysis, this investigation shows that a scaling factor of 3 is the preferred option, as it balances the lower computational cost against the accuracy of the mean solution. We should also take note, however that care should be taken in the selection of the time step, especially when evaluating systems with low hematocrits, consisting of a few edges, or with fast dynamics.

Appendix B Network preprocessing

Skeletonised glomeruli in this study have capillary diameters defined at the endpoints of each edge. To fit the numerical framework, the conical frustums are first converted into circular cylinders with the same volume so that each edge has a constant diameter. From this, chains of degree-two nodes ($\deg(v) = 2$), with one inlet and one outlet edge, are collapsed into longer edges so that

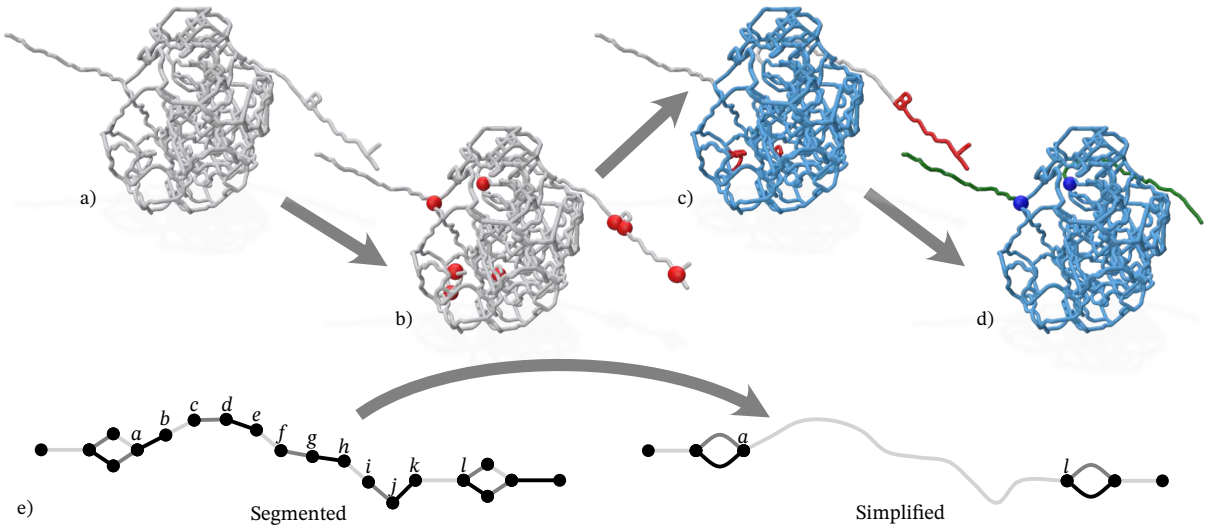

Fig. B11 The procedure used for simplifying the raw glomerulus network. The raw network, in panel a), is loaded into the script. Articulation points are identified in panel b) and used to extract the largest bi-connected component (BCC), indicated in blue in panel c). Here BCCs that do not contain nodes with $\deg(v) = 1$, i.e. self loops, and complex portions on the inlet sections are trimmed off the network, as shown in red. In panel d), the candidate inlet/outlet nodes with the largest cross-sectional area are retained alongside the inlet and outlet edges, shown in green. At runtime, these green edges are trimmed further so that glomerular network is analysed with minimal influence from the length of these inlet/outlet edges. Panel e) shows the simplification of edges with chains of $\deg(v) = 2$ nodes. The length and volume of the chain *a*-*l* are maintained after the removal of the node chain *b*-*k*, however, in the visualisations, the exact shape of the edge is approximate.

$\deg(v) \in \mathbb{N}/\{0, 2\}$ for all nodes v in the network. As before, the volume of the whole chain is maintained by adjusting the diameters of the simplified edge, while the removed vertices are retained as edge parameters for visualisation purposes. This process is illustrated in fig. B11e.

We are primarily interested in main connected components of the network corresponding to the core portion of the glomerulus. Due to imaging resolution and issues surrounding marker dye diffusion, the skeletonised network graph can, occasionally, have dead-end loops and multiple degree-one nodes that make for redundant portions of the graph and ambiguous inlet-outlet edges, respectively. In addition, the imaging of the glomerulus does not capture flow information, hence the edges selected as the inlet and outlet of the network must be labelled appropriately. Further processing is therefore required to transform these cases into a standard form.

A decomposition of the network into its *bi-connected components* identifies sub-graphs in which the removal of any node does not lead to the sub-graph becoming disconnected. These sub-graphs are connected together in the full network by nodes, known as *articulation points*, the removal of any one of which leads to a disconnection of the network main network. We identify the largest of these subcomponents and locate the intersection of the articulation points with this component. For each articulation point, either the smaller sub-component does not have nodes with $\deg(v) = 1$, in which case it is removed, or it does, in which case the articulation point is labelled as a candidate inlet/outlet node. For all of these candidate nodes, the one with the largest total cross-sectional area is taken to be the inflow, with the second-largest taken to be the outflow, which, in the cases considered in this paper, was possible to do without ambiguity. All other biconnected components are removed, and short linear segment edges are added at the inflow and outflow nodes.

Appendix C Filtration model

The main assumption introduced in eq. (9) is that the pressure distribution inside the capillary

is invariant to the positions of the RBCs, and that filtration performance measure used solely depends on a mean pressure at the two nodes and the total number of RBCs in a vessel. In reality, the pressure profile on any given edge has a negative piecewise-constant pressure gradient along its length, due to the viscous resistance of the plasma flow with elevated pressure drops over shorter scales across the location of each RBC, where the parabolic Poiseuille flow profile is modified.

If eq. (8) is instead interpreted in this continuous form for an edge with an RBC at the inlet, the filtration rate will initially be low, and, as the particle moves along the length of the edge, the pressure behind it will rise over an increasingly larger segment. In terms of the total filtration rate over the whole edge, this too would start out lower and then increase until the particle leaves the edge through the outlet, even though the mean pressure stays constant.

This discrepancy between this particle-tracking form and the form presented in eq. (9), is especially evident in cases where chains of degree-2 nodes are considered. With a single RBC circulating between the inlet and outlet node, the network performance will be constant in an edge with two nodes, but, as this edge is refined and subdivided into sub-sections, the instantaneous values will oscillate each time the RBC passes into the next sub-section of the edge. Furthermore, the pressure behind the RBCs is higher than in front, so the filtration is initially lower, and, as the RBC travels to the outlet, filtration increases.

Analysis of this issue, as well as the implementation of a continuous network filtration model (not included in this discussion), showed that, in simple networks at a fixed hematocrit, the discrepancy in the *instantaneous* filtration rate is quite noticeable. On the other hand, moving windowed averages of the outputs from both models showed that not only was the mean filtration rate captured well by the mean-pressure model in eq. (9), but also medium and long-term windowed averages, with the discrepancy tending to decrease as network complexity increased.

While the implementation of the more accurate filtration model might be desirable under certain conditions, the additional computational overhead of tracking and resolving the pressure profile in each edge is prohibitive for the kinds of problems that we wish to consider. For this reason, we are satisfied that, while better models can be devised, the model used in this paper will capture the primary and leading-order effects of filtration in our networks, enabling us to make reliable comparisons between different networks.

References

Drumond, M.C., Deen, W.M.: Analysis of pulsatile pressures and flows in glomerular filtration **261**(3), 409–419 (1991) https://doi.org/10.1152/ajprenal.1991.261.3.F409

Feher, J.: 7.3 - glomerular filtration. In: Quantitative Human Physiology, 2nd edn., pp. 705–714. Academic Press, Boston (2017). https://doi.org/10.1016/B978-0-12-800883-6.00070-7

Fung, Y.-C.: Stochastic flow in capillary blood vessels. Microvascular Research **5**(1), 34–48 (1973) https://doi.org/10.1016/S0026-2862(73)80005-6

Fung, Y.C., Zweifach, B.W.: Microcirculation: Mechanics of Blood Flow in Capillaries. Annual Review of Fluid Mechanics **3**(1), 189–210 (1971) https://doi.org/10.1146/annurev.fl.03.010171.001201

Goligorsky, M.S.: Glomerular microcirculation: Implications for diabetes, preeclampsia, and kidney injury. Acta Physiologica **239**(3), 14048 (2023) https://doi.org/10.1111/apha.14048

Hildebrand, T., Rüegsegger, P.: A new method for the model-independent assessment of thickness in three-dimensional images. Journal of Microscopy **185**(1), 67–75 (1997)

Hagberg, A.A., Schult, D.A., Swart, P.J.: Exploring network structure, dynamics, and function using networkx. In: Varoquaux, G., Vaught, T., Millman, J. (eds.) Proceedings of the 7th Python in Science Conference, Pasadena, CA USA, pp. 11–15 (2008)

Hyakutake, T., Tsutsumi, Y., Miyoshi, Y., Yasui, M., Mizuno, T., Tateno, M.: Red Blood Cell Partitioning Using a Microfluidic Channel with Ladder Structure. Micromachines **14**(7), 1421 (2023) https://doi.org/10.3390/mi14071421

Hudetz, A.G.: Blood Flow in the Cerebral Capillary Network: A Review Emphasizing Observations with Intravital Microscopy. Microcirculation **4**(2), 233–252 (1997) https://doi.org/10.3109/10739689709146787

Kuo, W., Rossinelli, D., Schulz, G., Wenger, R.H., Hieber, S., Müller, B., Kurtcuoglu, V.: Terabyte-scale supervised 3D training and benchmarking dataset of the mouse kidney. Scientific Data **10**(1), 510 (2023) https://doi.org/10.1038/s41597-023-02407-5

Merlo, A., Berg, M., Duru, P., Risso, F., Davit, Y., Lorthois, S.: A few upstream bifurcations drive the spatial distribution of red blood cells in model microfluidic networks **18**(7), 1463–1478 https://doi.org/10.1039/d1sm01141c

Nyengaard, J.R., Bendtsen, T.F.: Glomerular number and size in relation to age, kidney weight, and body surface in normal man. The Anatomical Record **232**(2), 194–201 (1992) https://doi.org/10.1002/ar.1092320205

Obrist, D., Weber, B., Buck, A., Jenny, P.: Red blood cell distribution in simplified capillary networks. Philosophical Transactions of the Royal Society A: Mathematical, Physical and Engineering Sciences **368**(1921), 2897–2918 (2010) https://doi.org/10.1098/rsta.2010.0045

Pries, A.R., Neuhaus, D., Gaehtgens, P.: Blood viscosity in tube flow: dependence on diameter and hematocrit. American Journal of Physiology-Heart and Circulatory Physiology **263**(6), 1770–1778 (1992)

Pozrikidis, C.: Numerical Simulation of Blood Flow Through Microvascular Capillary Networks. Bulletin of Mathematical Biology **71**(6), 1520–1541 (2009) https://doi.org/10.1007/s11538-009-9412-z

Pries, A.R., Secomb, T.W.: Microvascular blood viscosity in vivo and the endothelial surface layer. American Journal of Physiology-Heart and Circulatory Physiology **289**(6), 2657–2664 (2005) https://doi.org/10.1152/ajpheart.00297.2005

Pries, A.R., Secomb, T.W., Gaehtgens, P., Gross, J.F.: Blood flow in microvascular networks. Experiments and simulation. Circulation Research **67**(4), 826–834 (1990) https://doi.org/10.1161/01.RES.67.4.826

Sharp, N., et al.: Polyscope. www.polyscope.run (2019)

Schmid, F., Barrett, M.J.P., Obrist, D., Weber, B., Jenny, P.: Red blood cells stabilize flow in brain microvascular networks. PLOS Computational Biology **15**(8), 1007231 (2019) https://doi.org/10.1371/journal.pcbi.1007231

Schmid, F., Reichold, J., Weber, B., Jenny, P.: The impact of capillary dilation on the distribution of red blood cells in artificial networks. American Journal of Physiology-Heart and Circulatory Physiology **308**(7), 733–742 (2015) https://doi.org/10.1152/ajpheart.00335.2014

Starling, E.H.: On the Absorption of Fluids from the Connective Tissue Spaces. The Journal of Physiology **19**(4), 312–326 (1896) https://doi.org/10.1113/jphysiol.1896.sp000596

Schmid, F., Tsai, P.S., Kleinfeld, D., Jenny, P., Weber, B.: Depth-dependent flow and pressure characteristics in cortical microvascular networks. PLOS Computational Biology **13**(2), 1005392 (2017) https://doi.org/10.1371/journal.pcbi.1005392

Terasaki, M., Brunson, J.C., Sardi, J.: Analysis of the three dimensional structure of the kidney glomerulus capillary network. Scientific Reports **10**(1), 20334 (2020) https://doi.org/10.1038/s41598-020-77211-x

Wahl, E.M., Daniels, F.H., Leonard, E.F., Levinthal, C., Cortell, S.: A graph theory model of the glomerular capillary network and its development. Microvascular Research **27**(1), 96–109 (1984) https://doi.org/10.1016/0026-2862(84)90044-X

Wahl, E.M., Quintas, L.V., Lurie, L.L., Gargano, M.L.: A graph theory analysis of renal glomerular microvascular networks. Microvascular Research **67**(3), 223–230 (2004) https://doi.org/10.1016/j.mvr.2003.11.005

Woodcock, T.E., Woodcock, T.M.: Revised Starling equation and the glycocalyx model of transvascular fluid exchange: An improved paradigm for prescribing intravenous fluid therapy. British Journal of Anaesthesia **108**(3), 384–394 (2012) https://doi.org/10.1093/bja/aer515